ATLAS NOTE

ATLAS-CONF-2016-048

3rd August 2016

Search for top-squark pair production in final states with two tau leptons, jets, and missing transverse momentum in $\sqrt{s} = 13$ TeV pp collisions with the ATLAS detector

The ATLAS Collaboration

Abstract

A search for direct top-squark pair production in final states with two tau leptons, jets, and missing transverse momentum is presented. The analysis uses a dataset of proton–proton collisions with an integrated luminosity of 13.2 fb^{-1}, recorded with the ATLAS detector at the Large Hadron Collider at a centre-of-mass energy of $\sqrt{s} = 13$ TeV. No significant deviation from the Standard Model expectation is observed in the data. The results are interpreted using simplified models, and exclusion limits at 95 % confidence level on the sparticle masses are derived. Masses of the top squark up to 870 GeV and of the tau slepton up to 730 GeV are excluded.

ATLAS-CONF-2016-048
08 August 2016

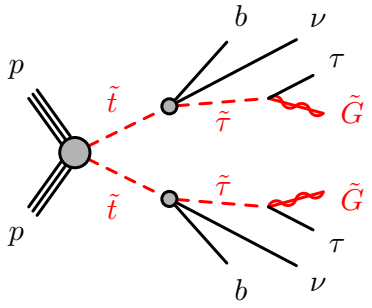

Figure 1: The simplified model targeted by the analysis presented in this note. The branching ratios are assumed to be 100 % for both decays, and all sparticles not appearing in this diagram are assumed to be too massive to be relevant for the observable kinematics.

1. Introduction

Supersymmetry (SUSY) [1–7] adds to the symmetries of the Standard Model (SM) [8] a symmetry connecting bosons and fermions, thereby providing answers to several of the open questions in the SM. It predicts the existence of new particles which differ in spin by one half-unit with respect to their SM partners. In models where R-parity is conserved [9], the superpartners of the SM particles (sparticles) are produced in pairs and the lightest supersymmetric particle (LSP) is stable, providing a viable candidate for dark matter.

This note studies Supersymmetry in a benchmark scenario motivated by gauge-mediated SUSY breaking (GMSB) [10–12] and natural gauge mediation (nGM) [13]. In this scenario, only three sparticles are assumed to be sufficiently light to be relevant in collider phenomenology: the lighter top squark $\tilde{t}_1$ (stop), the lighter tau slepton $\tilde{\tau}_1$ (stau), and a nearly massless gravitino $\tilde{G}$ as LSP ($m(\tilde{G}) < 1\,\text{GeV}$).

The search strategy is optimised using simplified models with this limited sparticle content, the varied parameters being the sfermion masses $m(\tilde{t}_1)$ and $m(\tilde{\tau}_1)$, assuming a branching ratio of 100 % for the decay illustrated in Figure 1: $\tilde{t}_1 \to b\tilde{\tau}_1\nu_\tau$ followed by $\tilde{\tau}_1 \to \tau\tilde{G}$.

The usual choice of the lightest neutralino $\tilde{\chi}_1^0$ as LSP would suggest a high branching ratio of $\tilde{t}_1 \to t\tilde{\chi}_1^0$, which has been studied elsewhere [14–19]. The stop is assumed to be light [20, 21] and directly pair-produced through the strong interaction. The search uses proton–proton (pp) collision data collected with the ATLAS detector at $\sqrt{s} = 13\,\text{TeV}$ in 2015 and early 2016, with a combined integrated luminosity of $13.2\,\text{fb}^{-1}$.

Previous analyses considering the same (ATLAS) or a comparable model (LEP) have set exclusion limits on the masses of $\tilde{t}_1$ and $\tilde{\tau}_1$ of 650 GeV [22] and 87 GeV [23], respectively. The higher centre-of-mass energy in Run 2 of the LHC increases the effective parton luminosity for the production of heavy particles, resulting in a higher sensitivity despite the lower integrated luminosity. In this note, events are considered only where one of the tau leptons decays hadronically, the other into a light lepton (electron or muon).

This note is structured as follows: Section 2 gives a brief description of the ATLAS detector. Section 3 defines the recorded and simulated events used in the analysis, Section 4 summarises the reconstruction of physics objects and the event selection. The background determination is described in Section 5, and the methods used to derive the corresponding systematic uncertainties are discussed in Section 6. Section 7

presents the results and their interpretation in the benchmark scenario. The note concludes with a brief summary in Section 8.

2. ATLAS Detector

The ATLAS experiment [24] is a multi-purpose particle detector with a forward–backward symmetric cylindrical geometry and nearly 4π coverage in solid angle.[1] The interaction point is surrounded by an inner detector, a calorimeter system, and a muon spectrometer.

The inner detector provides precision tracking of charged particles for pseudorapidities $|\eta| < 2.5$ and is surrounded by a superconducting solenoid providing a 2 T axial magnetic field. It consists of pixel and silicon-microstrip detectors inside a transition radiation tracker. One significant upgrade for the $\sqrt{s} = 13$ TeV running period is the presence of the Insertable B-Layer [25], an additional pixel layer close to the interaction point, which provides high-resolution hits at small radii to improve the tracking performance.

In the pseudorapidity region $|\eta| < 3.2$, high-granularity lead/liquid-argon (LAr) electromagnetic (EM) sampling calorimeters are used. A steel/scintillator tile calorimeter measures hadron energies for $|\eta| < 1.7$. The end-cap and forward regions, spanning the region $1.5 < |\eta| < 4.9$, are instrumented with LAr calorimeters for both the EM and hadronic energy measurements.

The muon spectrometer consists of superconducting toroids and a system of trigger and precision-tracking chambers, which provide triggering and tracking capabilities in the ranges $|\eta| < 2.4$ and $|\eta| < 2.7$, respectively.

A two-level trigger system is used to select events of interest [26]. The first trigger level is implemented in hardware and uses only a subset of the detector information. It is followed by the software-based High-Level Trigger stage, which can run offline reconstruction and calibration software, reducing the event rate to about 1 kHz.

3. Dataset and Simulated Event Samples

The analysis uses 13.2 fb^{-1} of pp collision data recorded in 2015 and 2016 at $\sqrt{s} = 13$ TeV with the ATLAS detector, after the application of beam, detector and data quality requirements. The preliminary uncertainty on the integrated luminosity of the dataset is 2.9 %. It is derived following a methodology similar to that detailed in Refs. [27, 28]. In the analysis, each simulated process is weighted according to the integrated luminosity of data as well as the cross-section estimate with the highest accuracy available.

Samples of simulated signal events have been generated for stop and stau masses of up to 950 GeV with $m(\tilde{t}_1) - m(\tilde{\tau}_1) > 10$ GeV, using MadGraph5_aMC@NLO v2.2.3 [29] with the NNPDF2.3 LO [30]

[1] ATLAS uses a right-handed coordinate system with its origin at the nominal interaction point (IP) in the centre of the detector and the z-axis along the beam pipe. The x-axis points from the IP to the centre of the LHC ring, and the y-axis points upward. Cylindrical coordinates (r, ϕ) are used in the transverse plane, ϕ being the azimuthal angle around the beam pipe. The pseudorapidity is defined in terms of the polar angle θ as $\eta = -\ln\tan(\theta/2)$. Rapidity is defined as $y = 0.5 \ln\left[(E + p_z)/(E - p_z)\right]$ where E denotes the energy and p_z is the component of the momentum along the beam direction.

parton density function (PDF) set for the stop production and three-body decay. The spin correlation between the b-quark and the neutrino are accounted for by MadGraph. All subsequent decays, as well as the hadronisation, are simulated with Pythia 8.186 [31], and the modelling of heavy-flavour decays is improved by EvtGen 1.2.0 [32].

Signal cross sections are calculated to next-to-leading order in the strong coupling constant, adding the resummation of soft gluon emission at next-to-leading-logarithmic accuracy (NLO+NLL) [33–35]. The nominal cross section and the uncertainty are taken from an envelope of cross-section predictions using different PDF sets and factorisation and renormalisation scales, as described in Ref. [36].

Top-antitop-quark production and single-top-quark production events are generated using Powheg-Box r3026 [37], with the CT10 PDF set [38] and the Perugia2012 set of tuned parameters (tune) of the Monte Carlo (MC) programs [39]. Parton fragmentation and hadronisation are simulated with Pythia 6.428 [40]. The modelling of heavy-flavour decays is improved using EvtGen 1.2.0. The overall cross section is normalised to NNLO+NNLL accuracy [41] for $t\bar{t}$, to NLO+NNLL accuracy for the single-top-quark Wt-channel [42], and to NLO for the t- and s-channels [43].

Events containing a W or Z boson with associated jets are generated at NLO with massive b/c-quarks using Sherpa 2.2 [44,45], with an internal PDF set based on CT10. Diboson events ($VV = WW/WZ/ZZ$) are generated using Sherpa 2.1 using the CT10 PDF set.

Top-antitop-quark production with an additional W or Z boson ($t\bar{t} + V$) is generated using MadGraph v2.2.2, fragmentation and hadronisation are simulated with Pythia 8.186. The ATLAS underlying-event tune A14 [46] is used together with the NNPDF2.3 LO PDF set, the cross sections are normalised to NLO accuracy [47, 48]. Simulation of top-antitop-quark with associated Higgs-boson production ($t\bar{t} + H$) is performed with MG5_aMC@NLO v2.2.2 interfaced to Herwig 2.7.1 [49]. The UEEE5 underlying event tune [50] is used together with the CTEQ6L1 [51] (matrix element) and CT10 (parton shower) PDF sets. Events are normalised to cross sections calculated at NLO QCD [52].

All simulated background samples are passed through a full GEANT4 [53] simulation of the ATLAS detector [54]. The signal samples are passed through a fast detector simulation based on a parametrisation of the performance of the ATLAS electromagnetic and hadronic calorimeters [55] and on GEANT4 elsewhere. All simulated signal and background samples are reconstructed using the same software as for the data.

The effect of additional pp interactions per bunch crossing ("pile-up") as a function of the instantaneous luminosity is taken into account by overlaying simulated minimum-bias events according to the observed distribution of the number of pile-up interactions in data. Event weights are used to make the distribution of the average number of simultaneous pp collisions in the simulated events match that of the recorded data.

4. Event Reconstruction and Selection

The analysis uses events with exactly one identified hadronic tau lepton and exactly one electron or muon, while events with additional leptons are vetoed. For electrons and muons, this veto uses a looser ("baseline") definition, while the selected electron or muon must fulfil tighter ("signal") criteria.

Electron candidates are reconstructed from clusters of calorimeter cells in the EM calorimeter matched to tracks in the inner detector. Although the electron η is derived from the EM clusters, it is limited to

the tracker acceptance, $|\eta_{\text{cluster}}| < 2.47$. A likelihood-based electron identification [56] is used to select electron candidates. Baseline (signal) electrons are selected using the loose (tight) working point and must have transverse momentum $p_{\text{T}} > 10\,\text{GeV}$ ($> 25\,\text{GeV}$). Signal electrons additionally must satisfy requirements on their isolation and on the impact parameters, $|d_0/\sigma(d_0)| < 5$ and $|z_0 \sin(\theta)| < 0.5\,\text{mm}$, where the longitudinal and transverse impact parameters z_0 and d_0 are calculated with respect to the primary vertex.

Muon candidates are reconstructed by combining the information of the muon spectrometer and the inner detector. Baseline muons must have $p_{\text{T}} > 10\,\text{GeV}$, $|\eta| < 2.5$ and fulfil medium quality criteria [57]. Signal muons further must have $p_{\text{T}} > 25\,\text{GeV}$, and satisfy isolation and impact parameter requirements, $|d_0/\sigma(d_0)| < 3$ and $|z_0 \sin(\theta)| < 0.5\,\text{mm}$. Events containing a baseline muon with a poorly measured charge-to-momentum ratio ($\sigma(q/p) \,/\, |q/p| > 0.2$) are rejected, as are events containing baseline muons with high impact parameters ($|z_0| > 1\,\text{mm}$ or $|d_0| > 0.2\,\text{mm}$), as these may originate from cosmic rays.

Jets are reconstructed using the anti-k_t algorithm [58] with distance parameter $R = 0.4$ using topological clusters of calorimeter cells as input, and are calibrated using the EM+JES+GSC scheme [59]. Selected jets must fulfil $p_{\text{T}} > 20\,\text{GeV}$ and $|\eta| < 2.8$. To suppress jets from simultaneous pp interactions, jets with $p_{\text{T}} < 60\,\text{GeV}$ and $|\eta| < 2.4$ are required to have a jet-vertex-tagger [60] output larger than 0.59, indicating that a significant fraction of their associated tracks is originating from the primary vertex.

Jets containing b-hadrons (b-jets) are identified using the MV2c10 algorithm, a multivariate discriminant making use of track impact parameters and reconstructed secondary vertices [61]. Candidate b-jets are required to have $p_{\text{T}} > 20\,\text{GeV}$ and $|\eta| < 2.5$. A working point with an average b-tagging efficiency of 77 % for simulated $t\bar{t}$ events is used [62, 63]. The rejection factors for light-quark jets, c-quark jets and hadronically decaying tau leptons are approximately 134, 6 and 55, respectively.

The reconstruction of hadronically decaying tau leptons is seeded by jets reconstructed with the anti-k_t algorithm with distance parameter $R = 0.4$, and considers only jets with $p_{\text{T}} > 10\,\text{GeV}$ and $|\eta| < 2.5$ [64]. The reconstructed energy of the hadronic tau leptons is calibrated using tau-energy-scale corrections based on simulation, which are derived independently from jet-energy-scale corrections. Tau leptons are required to have $p_{\text{T}} > 20\,\text{GeV}$ and $|\eta| < 2.47$, excluding the transition region between the barrel and end-cap calorimeters ($1.37 < |\eta| < 1.52$). Tau leptons are associated to tracks and subsequently to a primary vertex. They must have 1 or 3 tracks (prongs) and a total electric charge of the tracks of ± 1. For an improved discrimination between hadronically decaying tau leptons and jets, a multivariate identification algorithm based on the Boosted Decision Tree method is used. The medium working point is used, with 55 % (40 %) efficiency for 1-prong (3-prong) tau leptons. To discriminate between tau leptons and electrons, an overlap-based veto is used, with a tau efficiency of 95 %.

The missing transverse momentum, denoted as $E_{\text{T}}^{\text{miss}}$, is defined as the magnitude of the negative vectorial sum of the p_{T} of all calibrated jets, electrons, muons, and tau leptons, with an additional soft term. The soft term is constructed from all tracks that are not associated with any physics object, and that are associated to the primary vertex. In this way, the missing transverse momentum is adjusted for the best calibration of the jets and the other identified physics objects above, while maintaining pile-up independence in the soft term [65].

To avoid labelling the same detector signature as more than one object, an overlap removal procedure is applied. Tau candidates close to a baseline electron or muon ($\Delta R < 0.2$, where $\Delta R := \sqrt{(\Delta y)^2 + (\Delta\phi)^2}$) are removed, as are electrons sharing a track with a muon. For electrons close to a jet ($\Delta R < 0.4$), the electron is removed, except when $\Delta R < 0.2$ and the jet is not b-tagged, in which case the jet is removed. Any remaining jet within $\Delta R < 0.4$ of a muon or tau lepton is removed.

Variable	SR requirement
$N_{b\text{-jet}}$	≥ 1
$E_{\mathrm{T}}^{\mathrm{miss}}$	$> 180\,\mathrm{GeV}$
$p_{\mathrm{T}}(\tau)$	$> 70\,\mathrm{GeV}$
$m_{\mathrm{T2}}(\ell,\tau)$	$> 100\,\mathrm{GeV}$

Table 1: Selection requirements for the signal region (SR).

To account for an imperfect modelling of the reconstruction and identification efficiencies and energy scales of physics objects by the simulation, each reconstructed object in a simulated event receives a weight ("scale factor"). Scale factors needed to correctly model object vetoes, for example for incorrectly b-tagged light jets, are included as well. The product of all object scale factors is applied as an event weight.

Events are selected with single-electron and single-muon triggers, using the lowest unprescaled p_{T} thresholds available. These triggers are at their maximal efficiency for the requirements on the lepton transverse momentum imposed by the event selection described below. The events are required to have a reconstructed vertex [66] with at least two associated tracks with $p_{\mathrm{T}} > 400\,\mathrm{MeV}$. The vertex with the highest sum of squared track transverse momenta is used as primary vertex.

All events must pass a common preselection, which requires exactly one selected tau lepton and one light lepton, which further needs to correspond to the single-lepton trigger object. Events with additional baseline leptons are rejected. The tau lepton and the light lepton must have opposite charge. Two jets, the leading one with $p_{\mathrm{T}} > 50\,\mathrm{GeV}$, are required.

Table 1 shows the selection requirements defining the signal region (SR), which is optimised to reject the background as much as possible while keeping a good signal acceptance. The most important variable in the SR definition is $m_{\mathrm{T2}}(\ell,\tau)$, which is a variant of the stransverse mass m_{T2}, defined as:

$$m_{\mathrm{T2}}^2 = \min_{\vec{q}_1+\vec{q}_2=\vec{E}_{\mathrm{T}}^{\mathrm{miss}}} \left[\max\left\{m_{\mathrm{T}}^2(\vec{p}_1,\vec{q}_1), m_{\mathrm{T}}^2(\vec{p}_2,\vec{q}_2)\right\}\right] \leq M^2, \tag{1}$$

where M is the mass of two identical intermediate particles both decaying into one visible and one invisible particle [67–69]. For $m_{\mathrm{T2}}(\ell,\tau)$, the four-momenta of the light lepton and the hadronic tau lepton are used as inputs, and the invisible particles are assumed to be massless. In this expression, $m_{\mathrm{T}}(\ell)$ is the transverse mass, computed from $E_{\mathrm{T}}^{\mathrm{miss}}$, the p_{T} of the light lepton, and the angle between them in the transverse plane. This setup targets $t\bar{t}$ events, with W bosons as the intermediate particles, and therefore $m_{\mathrm{T2}}(\ell,\tau)$ is bounded from above by the W-boson mass, while the signal has a much broader distribution. In addition to $m_{\mathrm{T2}}(\ell,\tau)$, the invariant mass of the tau lepton and the light lepton, $m(\ell,\tau)$, is used in the definition of control regions (CR), each of which is designed to be enriched in a certain type of background process.

5. Background Estimation

The general strategy for the estimation of the SM background processes in the signal region is to use a data-driven normalisation of the expected contributions from $t\bar{t}$ and W+jets in dedicated control regions. The contributions of all background processes are taken into account in a simultaneous fit of all control

Variable	CR $t\bar{t}$-Real	CR $t\bar{t}$-Fake	CR $t\bar{t}$-SS	CR W
$N_{b\text{-jet}}$	≥ 1	≥ 1	≥ 1	0
$E_{\mathrm{T}}^{\mathrm{miss}}$	> 180 GeV	> 120 GeV	> 150 GeV	> 100 GeV
$p_{\mathrm{T}}(\tau)$	> 70 GeV	> 70 GeV	> 20 GeV	< 90 GeV
$m_{\mathrm{T2}}(\ell,\tau)$	< 60 GeV	$20\,\mathrm{GeV} < m_{\mathrm{T2}}(\ell,\tau) < 60\,\mathrm{GeV}$	< 60 GeV	< 60 GeV
$m_{\mathrm{T}}(\ell)$	> 100 GeV	< 100 GeV	—	< 80 GeV
$m(\ell,\tau)$	—	—	—	> 80 GeV

Table 2: Definitions of the control regions used in the background fit to derive data-driven normalisation factors. The alternative CR $t\bar{t}$-SS is used to derive systematic uncertainties in the normalisation factor for $t\bar{t}$ events with fake tau leptons.

regions, where the normalisation of backgrounds with dedicated control regions are floating parameters. The other backgrounds are taken from MC simulation and fixed to their nominal cross sections in the fit.

Two different categories of SM background processes yielding detector signatures with one hadronic tau decay and one light lepton can be distinguished. The first category contains processes which give two real tau leptons or one real tau lepton and one real light lepton, mainly $t\bar{t}$, $Z+$jets, and diboson events. The second category includes processes which have only one real lepton, dominantly $W+$jets. As the probability to misidentify the detector signature of any object as a hadronically decaying tau lepton (yielding a fake tau lepton) is much higher than that to mistake some object as a light lepton, the fake background will mostly be events where the tau lepton is a fake and the light lepton is real rather than vice versa. After applying the signal-region selection, the expected SM background is dominated by events from $t\bar{t}$ where the tau lepton is a fake. Subdominant contributions are $t\bar{t}$ events with a real tau lepton and events with production of $t\bar{t}$ in association with a vector boson.

As the quality of the modelling of the $t\bar{t}$ background by the simulation may be different for events with real and with fake tau leptons, the background estimate for $t\bar{t}$ events is split into two separate estimates, one for $t\bar{t}$ events with a fake tau lepton and one for $t\bar{t}$ events with a real tau lepton, as determined from simulation by matching the reconstructed tau object to the truth information. The background from $t\bar{t}$ events is then normalised using two control regions, referred to as CR $t\bar{t}$-Real and CR $t\bar{t}$-Fake. The definitions of these control regions are given in Table 2. Both CRs predominantly select $t\bar{t}$ events with a real tau lepton in the final state, 79 % and 58 % of selected events before the background fit, respectively, but only CR $t\bar{t}$-Fake has a significant fraction of events with a jet misidentified as a hadronically decaying tau lepton (29 %; whereas only 2 % in CR $t\bar{t}$-Real). This separation is achieved foremost by the m_{T} requirement, where the lower bound suppresses the contribution of events with a fake tau lepton in CR $t\bar{t}$-Real. The definition of CR $t\bar{t}$-Fake reverts the m_{T} requirement of CR $t\bar{t}$-Real, thereby selecting a disjoint set of events that allows both contributions (fake and real) to be normalised independently. The relaxed $E_{\mathrm{T}}^{\mathrm{miss}}$ requirement for CR $t\bar{t}$-Fake is necessary to obtain a sufficient event yield. Other selected events entering the $t\bar{t}$ control regions are mostly from single-top-quark production, and signal events are suppressed by imposing an upper bound on the $m_{\mathrm{T2}}(\ell,\tau)$ variable. Figures 2 and 3 show kinematic distributions in the $t\bar{t}$ CRs for several variables used in the event selection. Good agreement between the background expectation and data is observed.

In addition to the $t\bar{t}$ control regions, a control region for the normalisation of $W+$jets events is used as in the Run-1 analysis, although this background has become less relevant in the signal region with the

	CR $t\bar{t}$-Real	CR $t\bar{t}$-Fake	CR W+jets
Observed events	150	190	1257
Total expected background	150 ± 12	190 ± 13	1260 ± 40
$t\bar{t}$ (fake τ)	7 ± 5	102 ± 29	270 ± 140
$t\bar{t}$ (real τ)	107 ± 25	67 ± 28	56 ± 26
single-top	31 ± 19	14 ± 10	35 ± 6
diboson	3.0 ± 0.7	2.2 ± 0.4	61 ± 8
W+jets	$0.08 \pm {}^{0.13}_{0.08}$	2.3 ± 1.5	780 ± 150
Z+jets	0.18 ± 0.07	1.0 ± 0.5	49 ± 22
$t\bar{t}+V$	1.54 ± 0.25	0.78 ± 0.14	0.95 ± 0.29
$t\bar{t}+H$	0.40 ± 0.05	0.43 ± 0.05	0.17 ± 0.05

Table 3: Expected event yields obtained from the background fit, and observed numbers of events in data in the control regions for the $t\bar{t}$ and W+jets background processes, given for an integrated luminosity of 13.2 fb^{-1}. The uncertainties include both statistical and systematic uncertainties.

improved tau identification in Run 2. The definition of this control region is also given in Table 2, the main difference with respect to the other control regions and the signal region being the selection of events with no b-tagged jets.

Table 3 lists the observed and expected yields in the control regions for each background source. The normalisation factors are obtained from the background fit as the ratio of the fitted event yield over the nominal MC expectation. The normalisation factor for W+jets is $\mu_W = 1.15 \pm 0.29$. For the $t\bar{t}$ background, there are two normalisation factors, $\mu_{\text{real}} = 0.74 \pm 0.41$ and $\mu_{\text{fake}} = 2.22 \pm 1.11$. The different normalisation factors account for differences in how well effects of the tau identification are modelled for real taus and for fake taus. The uncertainties include both statistical and systematic contributions (cf. Section 6).

The contribution of multi-jet events fulfilling the SR and CR requirements was verified to be negligible using the "same-sign method". This method assumes that events from multi-jet processes are equally likely to pass an opposite-sign and a same-sign selection (opposite- and same-sign referring to the relative electrical charge of the two leptons required in the selection) because there is no charge correlation between the two fake leptons within the event. The expected event yield from SM processes in the same-sign selection is subtracted from the observed number of events in data, and the result is used to estimate the number of multi-jet events in the opposite-sign selection. The contribution of multi-jet events to the $t\bar{t}$ control regions using this method was found to be of the order of one percent or less.

5.1. Validation of the Background Estimate

Events from $t\bar{t}$ pair production with a fake tau lepton are the dominant background process in the signal region. To assess the robustness of the estimate for this background process, alternative ways to determine its normalisation factor μ_{fake} have been considered.

A third CR for the $t\bar{t}$ background, CR $t\bar{t}$-SS, is defined, in which it is required that the electron or muon now have the same charge as (rather than opposite to) the tau lepton. This region is used for an independent cross-check of the $t\bar{t}$ event yield with a fake tau lepton. In comparison to the other $t\bar{t}$ control regions,

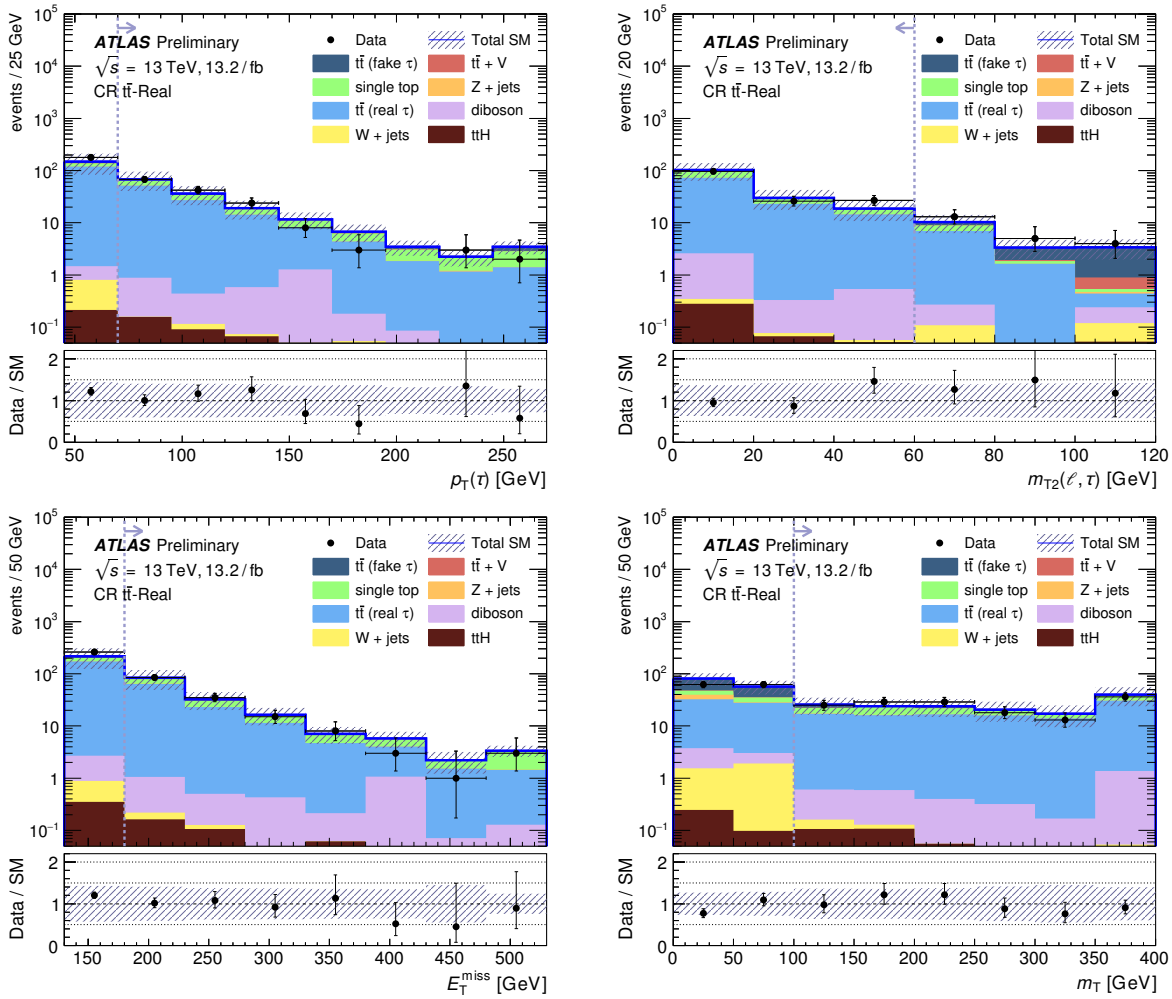

Figure 2: Comparison of data and simulation in CR $t\bar{t}$-Real for tau p_T (top left), $m_{T2}(\ell,\tau)$ (top right), E_T^{miss} (bottom left), and m_T (bottom right) after the fit. The plots show the distributions before applying the selection requirement on the respective variable. The requirements defining the control region are indicated by dashed lines and arrows. The error bands indicate the statistical and systematic uncertainties. The rightmost bin includes the overflow.

the requirement on $m_{T2}(\ell,\tau)$ is kept, but the requirement on the tau p_T is relaxed to increase event yields. The requirement on E_T^{miss}, on the other hand, has been kept rather high to suppress contributions from multi-jet events.

The central value, μ^0_{fake}, is determined from the nominal background-only fit setup in Table 3. A relative systematic uncertainty is derived by determining μ^{SS}_{fake} in a modified fit setup in which CR $t\bar{t}$-Fake is replaced by CR $t\bar{t}$-SS. The relative difference of the estimates $\Delta := \left(\mu^{SS}_{fake} - \mu^0_{fake}\right)/\mu^0_{fake}$ is treated as an additional systematic uncertainty on the normalisation of the $t\bar{t}$ background with fake tau leptons, i. e. $\mu_{fake} = \mu^0_{fake} \times (1 \pm |\Delta|)$. This uncertainty is applied on the estimate for $t\bar{t}$ events with a fake tau lepton in the signal region as an additional systematic uncertainty on top of the statistical uncertainty from the nominal background fit. From the ratio of fitted and MC expected yields, one obtains $\mu^{SS}_{fake} = 1.33 \pm 0.29$, where the uncertainty includes statistical and systematic uncertainties. The additional systematic uncertainty to be applied is thus $|\Delta| = |1.33 - 2.22| \,/\, 2.22 = 40\,\%$.

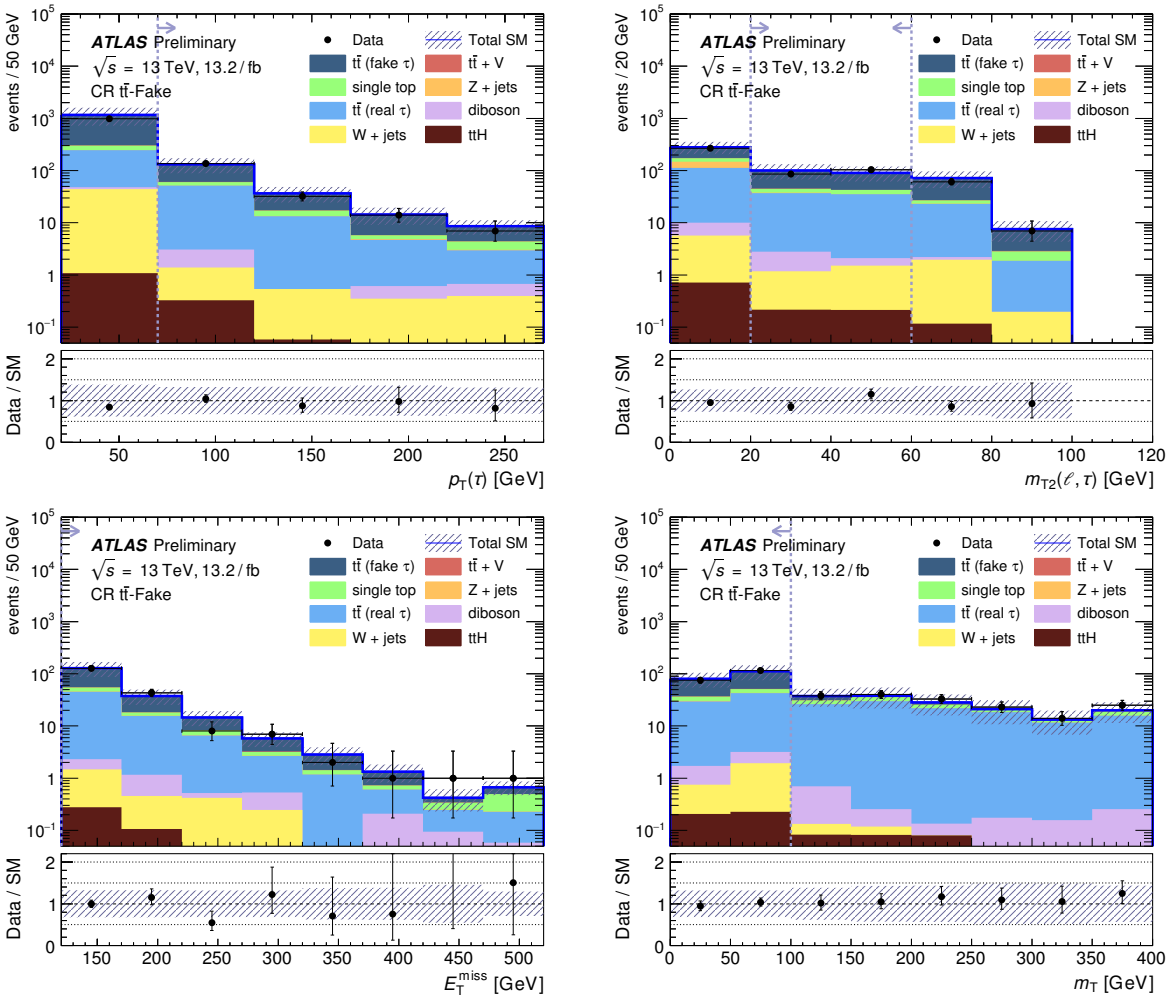

Figure 3: Comparison of data and simulation in CR $t\bar{t}$-Fake for tau p_{T} (top left), $m_{\mathrm{T2}}(\ell,\tau)$ (top right), $E_{\mathrm{T}}^{\mathrm{miss}}$ (bottom left), and m_{T} (bottom right) after the fit. The plots show the distributions before applying the selection requirement on the respective variable. The requirements defining the control region are indicated by dashed lines and arrows. The error bands indicate the statistical and systematic uncertainties. The rightmost bin includes the overflow.

As an additional cross-check, the two background fits have been repeated using a selection where loose tau leptons are used that do not pass the medium jet-discrimination requirements. This yields a disjoint set of events for both setups with an increased contribution from fake tau leptons. The resulting values are $\mu_{\mathrm{fake}}^{\mathrm{OS,loose}} = 0.78 \pm 0.42$ and $\mu_{\mathrm{fake}}^{\mathrm{SS,loose}} = 1.09 \pm 0.42$, compatible with the nominal scale factor μ_{fake} within the additional systematic uncertainty.

The correctness of the extrapolation from the control regions to the signal regions is confirmed using a set of validation regions with selection requirements between those of the control regions and the signal region. Table 4 lists the definitions of the four validation regions, two for the $t\bar{t}$ background and two for the W+jets background. The expected SM yields are in good agreement with the yields observed in data in all validation regions.

Variable	VR $t\bar{t}$-Real	VR $t\bar{t}$-Fake	VR W+jets (τ p_{T})	VR W+jets ($m_{\mathrm{T2}}(\ell,\tau)$)
$N_{b\text{-jet}}$	≥ 1	≥ 1	0	0
$E_{\mathrm{T}}^{\mathrm{miss}}$	> 180 GeV	> 150 GeV	> 100 GeV	> 100 GeV
$p_{\mathrm{T}}(\tau)$	> 70 GeV	> 70 GeV	> 90 GeV	< 90 GeV
$m_{\mathrm{T2}}(\ell,\tau)$	$60\,\mathrm{GeV} < m_{\mathrm{T2}}(\ell,\tau) < 100\,\mathrm{GeV}$		< 100 GeV	> 60 GeV
$m_{\mathrm{T}}(\ell)$	> 100 GeV	< 100 GeV	< 80 GeV	< 80 GeV
$m(\ell,\tau)$	–	–	> 80 GeV	> 80 GeV

Table 4: Selection requirements for the regions used to validate the background estimate.

6. Systematic Uncertainties

Several sources of systematic uncertainties are considered and enter all statistical tests. They can be grouped into experimental uncertainties, including detector-related uncertainties as well as an uncertainty of 2.9 % on the integrated luminosity of the analysed dataset, and theoretical uncertainties on the modelling of the relevant SM and SUSY processes.

The main sources of detector-related systematic uncertainties correspond to the jet and lepton energy calibrations and resolutions, the missing transverse momentum measurement as well as uncertainties on the b-jet and tau identification efficiencies and fake rates. For the missing transverse momentum, all jet and lepton uncertainties are propagated to the calculation and additional uncertainties on the soft-term contribution are included.

Theoretical uncertainties include uncertainties on production cross sections and PDF sets as well as uncertainties on the modelling of SM backgrounds, evaluated from samples of simulated events by varying MC generators or generator parameters. For $t\bar{t}$ and W+jets processes, only shape uncertainties are considered as the background normalisation is extracted from data. For both $t\bar{t}$ and single-top-quark production, uncertainties due to the hard-scattering generation are obtained by comparing Powheg+Herwig++ and aMC@NLO+Herwig++, while for fragmentation and hadronisation effects Powheg+Herwig++ is compared to Powheg+Pythia6. The modelling of the emission of additional partons in the initial and final states was evaluated using different parton-showering tunes as well as varying the renormalisation and factorisation scales. The uncertainty on the cross section for single-top-quark production is channel-dependent and up to 5 %, including the PDF uncertainty. The interference between $t\bar{t}$ and single-top-quark production in the Wt channel was estimated to be at most 65 % in any of the event selections used in this analysis by comparing simulated samples using either the diagram removal or the diagram subtraction technique. This uncertainty is applied to the full single-top-quark estimate in the SR. For the $t\bar{t}+V$ background, a 13 % cross-section uncertainty is used, including scale and PDF variations. Shape uncertainties on $t\bar{t}+V$ production are taken into account using particle-level samples of simulated events varying the renormalisation and factorisation scales. Systematic uncertainties on Z+jets and W+jets production are expected to have negligible impact due to the very low contributions to the signal region and the $t\bar{t}$ control regions. For diboson backgrounds, a global uncertainty of 6 % is included, accounting for uncertainties arising from the cross-section calculation and choice of PDF set. For the signal processes, the cross-section uncertainty is taken into account (cf. Section 3).

The systematic uncertainty on the background estimate in the signal region is dominated by the uncertainty on the $t\bar{t}$ modelling (53 %), followed by the uncertainty on the normalisation for $t\bar{t}$ events with a fake tau lepton of 49 %, which includes both the extrapolation from the CR and the additional systematic

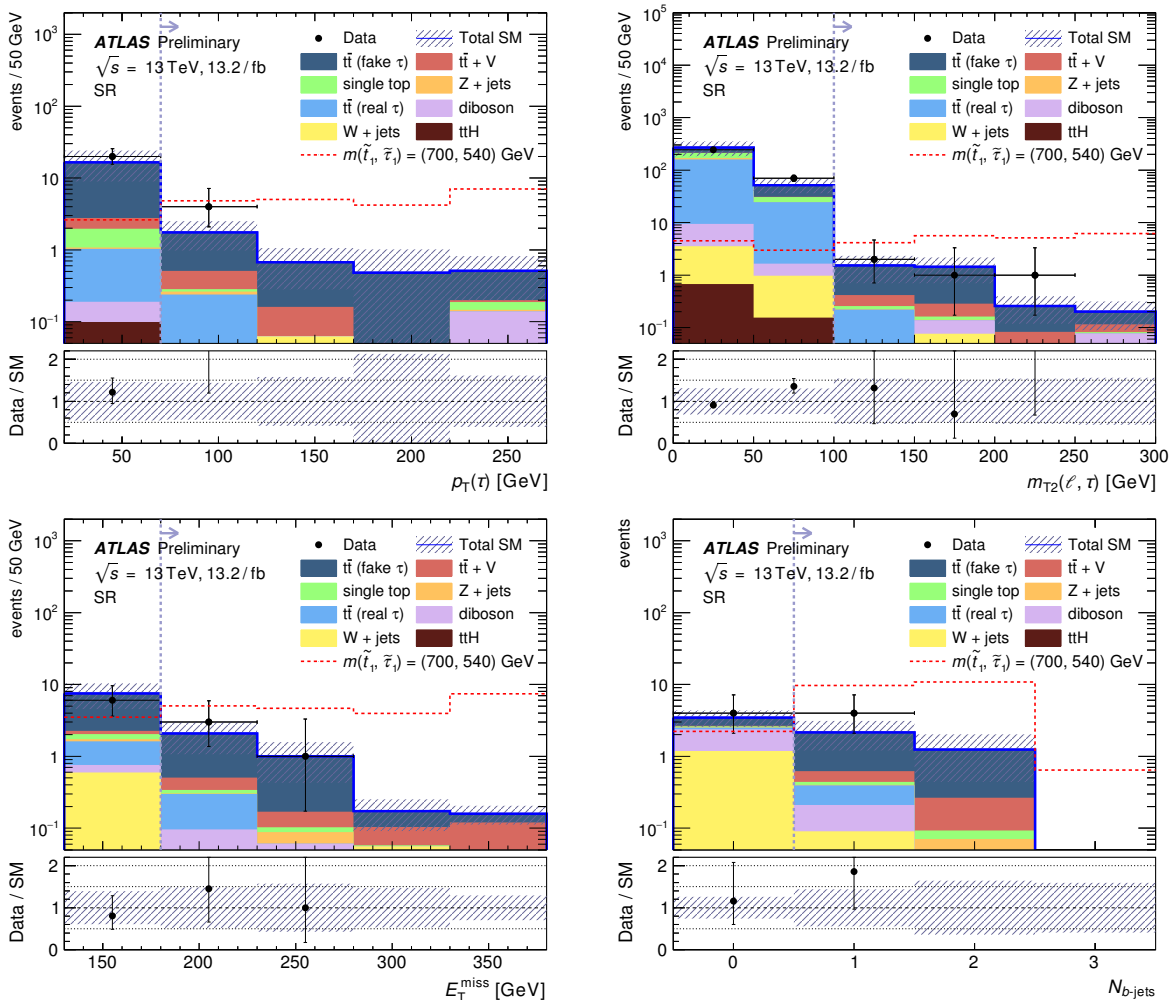

Figure 4: Distributions of the variables used in the signal-region (SR) definition after applying all signal-region requirements but the one on the respective variable: tau p_{T} (top left), $m_{\mathrm{T2}}(\ell,\tau)$ (top right), $E_{\mathrm{T}}^{\mathrm{miss}}$ (bottom left), and the number of b-tagged jets (bottom right), all after the fit. The plots show distributions for the expected background contributions from the fit (shaded histograms) and their sum (blue line), the observed data (black dots), and one example signal model (red dashed line) with $m(\tilde{t}_1) = 700\,\mathrm{GeV}$ and $m(\tilde{\tau}_1) = 540\,\mathrm{GeV}$. The requirements defining the signal region are indicated by vertical dashed lines and arrows. The error bands indicate the statistical and systematic uncertainties. The rightmost bin includes the overflow.

uncertainty on μ_{fake}. A 12 % contribution results from the uncertainty on the modelling of the pile-up distribution. All remaining systematic uncertainties combined have an effect of approximately 6 % on the estimated SR yield.

7. Results

Figure 4 shows distributions of the tau p_{T}, $m_{\mathrm{T2}}(\ell,\tau)$, $E_{\mathrm{T}}^{\mathrm{miss}}$, and the number of b-tagged jets after applying the signal-region selection except for the requirement on the variable itself. The events observed in data are shown as well as the expected contributions from SM backgrounds and a distribution for a benchmark

	SR
Observed events	4
Total background	3.4 ± 1.9
$t\bar{t}$ (fake τ)	2.5 ± 1.8
$t\bar{t} + V$	0.36 ± 0.19
$t\bar{t}$ (real τ)	$0.20^{+\ 0.24}_{-\ 0.20}$
diboson	$0.12^{+\ 0.20}_{-\ 0.12}$
W+jets	$0.07^{+\ 0.09}_{-\ 0.07}$
single-top	0.06 ± 0.06
$t\bar{t} + H$	0.05 ± 0.02
Z+jets	0.03 ± 0.01

Table 5: Expected numbers of events for the SM background processes from the fit and observed event yield in data for the signal region (SR), given for an integrated luminosity of 13.2 fb^{-1}. The uncertainties include both statistical and systematic uncertainties.

signal model. The $t\bar{t}$ and W+jets backgrounds are scaled according to the normalisation factors derived from the background fit.

The yields observed in data and the details of the expected number of background events in the signal region are listed in Table 5, together with their statistical and systematic uncertainties. Four events are observed in the signal region, to be compared to an expected background from SM processes of 3.4 ± 1.9 events. Thus, no significant excess is seen beyond the SM expectation. The overall agreement of expected and observed event yields in all control and validation regions and the signal region is summarised in a graphical way in Figure 5.

The results are used to derive model-independent exclusion limits and exclusion limits on the parameters of the simplified model, the mass of the scalar partner of the top quark and of the tau lepton. The HistFitter software framework [70] is used for the statistical interpretation of the result. It employs the profile-likelihood ratio as a test statistic [71] to compute exclusion limits with the CL$_s$ prescription [72] at 95 % confidence level (CL).

The expected and observed upper limits at 95 % CL on the number of non-SM events ($S^{95}_{\mathrm{exp\,/\,obs}}$) from the model-independent fit are $S_{\mathrm{exp}} = 6.6^{+2.5}_{-1.6}$ and $S^{95}_{\mathrm{obs}} = 7.3$, and the resulting limit on the signal cross section times efficiency is $\langle \epsilon\sigma \rangle^{95}_{\mathrm{obs}} = 0.55$ fb. The discovery p-value, i. e. the probability that the observed number of events is compatible with the background-only hypothesis, is $p_0 = 0.41$.

The limits on the mass parameters of the simplified model are displayed in Figure 6, comparing the expected and observed exclusion contours. In addition, the limit on the mass of the tau slepton from the LEP experiments and the limit from the Run-1 results of the corresponding ATLAS analysis are shown. As the number of events observed in data is slightly larger than the expected SM background, the observed exclusion reach is smaller than expected but within the one-sigma uncertainty band. Using 13.2 fb^{-1} of collision data at $\sqrt{s} = 13$ TeV, masses of the top squark up to 870 GeV and of the tau slepton up to 730 GeV are excluded at 95 % CL. This improves the Run-1 exclusion limit on the top-squark mass by up to 220 GeV.

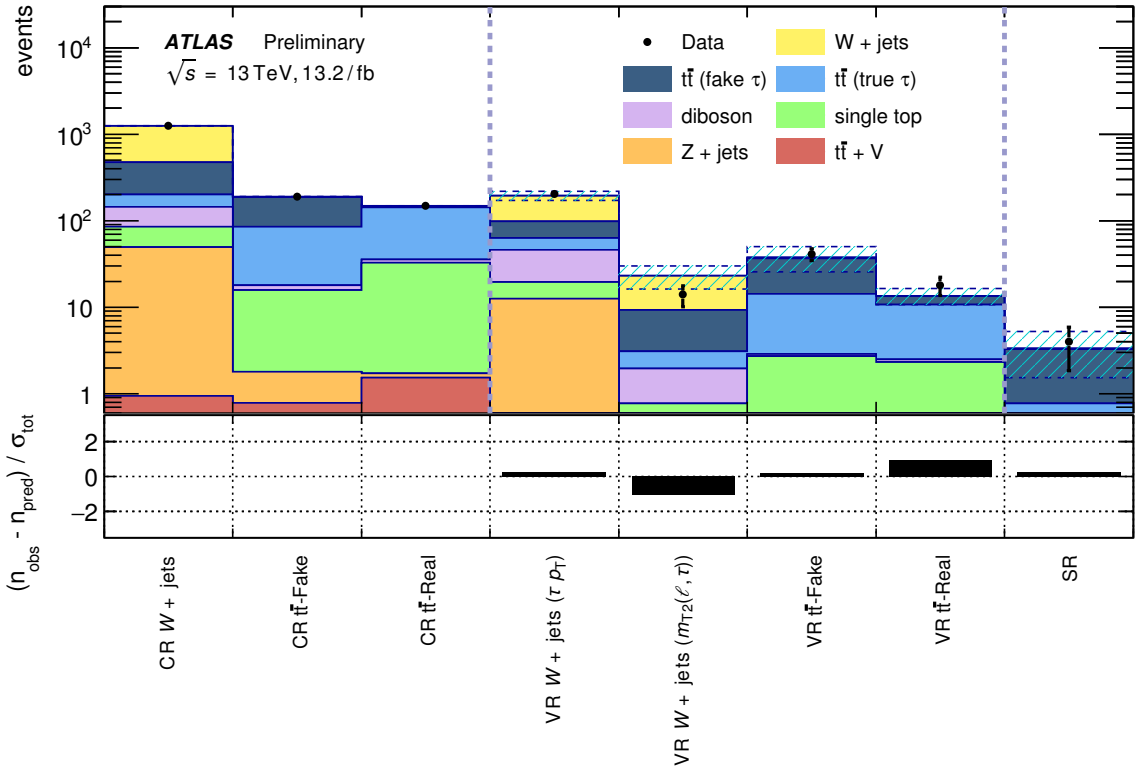

Figure 5: Comparison of expected background yields (shaded histograms) and event yields observed in data (dots) after the fit in all control (CR) and validation regions (VR) and the signal region (SR) defined in the analysis. The uncertainty band indicates the uncertainty on the total expected background yield. The lower panel shows the difference between expected background and observation in units of standard deviations, including both the uncertainty on the background as well as the Poisson error on the data, added in quadrature. By construction, after the fit the expected background yields in the control regions (first three bins on the left) agree exactly with the observed event yields in data.

8. Conclusion

This note reports results from a search for direct top-squark pair production in final states with two tau leptons, jets, and missing transverse momentum. The analysis is based on a dataset 13.2 fb^{-1} of proton–proton collisions, collected in 2015 and 2016 at a centre-of-mass energy of $\sqrt{s} = 13$ TeV, using events with one hadronic and one leptonic tau decay. No significant excess over the Standard Model expectation is observed in the signal region. The results are thus interpreted in terms of exclusion limits at 95 % confidence level on the masses of the scalar partners of the top quark and the tau lepton using simplified models. Masses of the top squark up to $m(\tilde{t}_1) = 870$ GeV and of the tau slepton up to $m(\tilde{\tau}_1) = 730$ GeV are excluded.

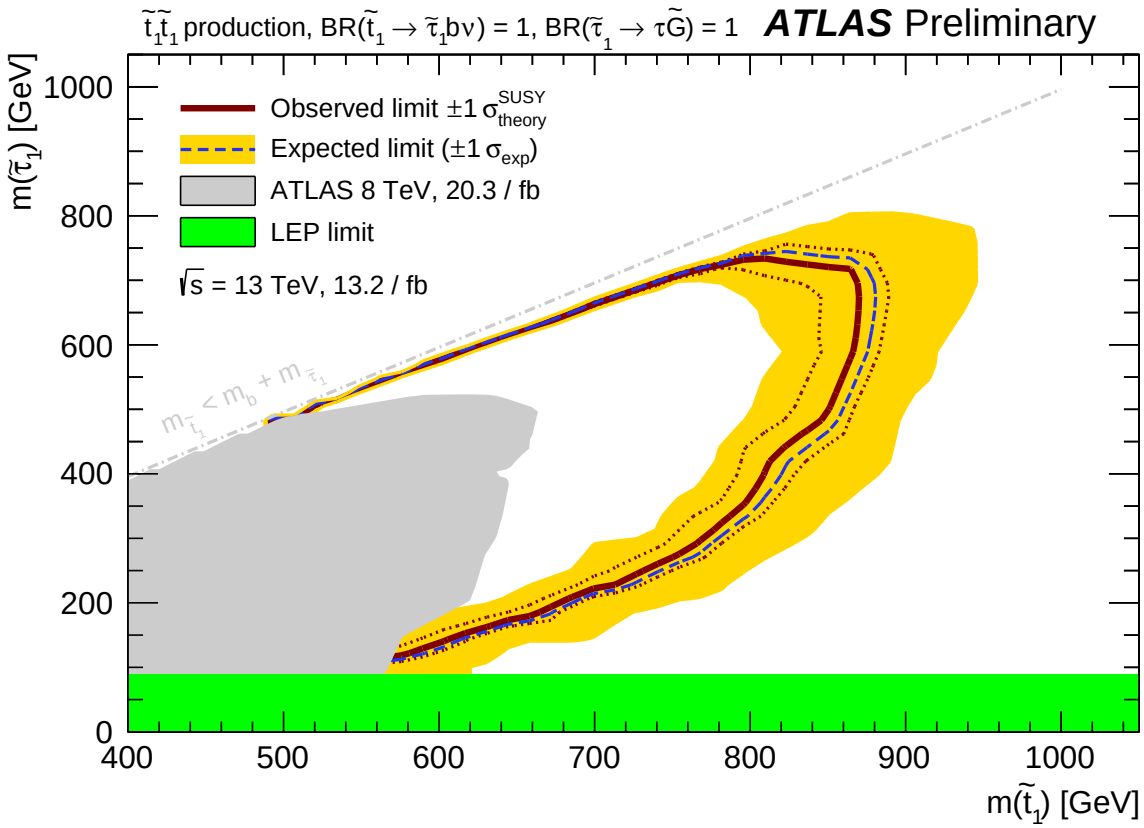

Figure 6: Expected and observed exclusion limits at 95 % CL for the simplified model and for 13.2 fb^{-1} of integrated luminosity at $\sqrt{s} = 13$ TeV. For comparison, the plot also includes the previous ATLAS exclusion contour [22] and the limit on the mass of the stau set by the LEP experiments [23].

References

[1] Yu. A. Golfand and E. P. Likhtman, *Extension of the Algebra of Poincare Group Generators and Violation of p Invariance*, JETP Lett. **13** (1971) 323–326, [Pisma Zh. Eksp. Teor. Fiz.13,452(1971)].

[2] D. V. Volkov and V. P. Akulov, *Is the Neutrino a Goldstone Particle?*, Phys. Lett. B **46** (1973) 109–110.

[3] J. Wess and B. Zumino, *Supergauge Transformations in Four-Dimensions*, Nucl. Phys. B **70** (1974) 39–50.

[4] J. Wess and B. Zumino, *Supergauge Invariant Extension of Quantum Electrodynamics*, Nucl. Phys. B **78** (1974) 1.

[5] S. Ferrara and B. Zumino, *Supergauge Invariant Yang-Mills Theories*, Nucl. Phys. B **79** (1974) 413.

[6] A. Salam and J. A. Strathdee, *Supersymmetry and Nonabelian Gauges*, Phys. Lett. B **51** (1974) 353–355.

[7] S. P. Martin, *A Supersymmetry primer*, arXiv:hep-ph/9709356 [hep-ph], [Adv. Ser. Direct. High Energy Phys.18,1(1998)].

[8] S. L. Glashow, Nucl. Phys. **22** (1961) 579; S. Weinberg, Phys. Rev. Lett. **19** (1967) 1264; A. Salam, Elementary Particle Theory, ed. N. Svartholm, (Almqvist and Wiksell, Stockholm, 1968), p. 367.

[9] G. Farrar and P. Fayet, *Phenomenology of the Production, Decay, and Detection of New Hadronic States Associated with Supersymmetry*, Phys. Lett. B **76** (1978) 575–579.

[10] M. Dine and W. Fischler, *A Phenomenological Model of Particle Physics Based on Supersymmetry*, Phys. Lett. B **110** (1982) 227.

[11] L. Alvarez-Gaume, M. Claudson, and M. B. Wise, *Low-Energy Supersymmetry*, Nucl. Phys. B **207** (1982) 96.

[12] C. R. Nappi and B. A. Ovrut, *Supersymmetric Extension of the SU(3) x SU(2) x U(1) Model*, Phys. Lett. B **113** (1982) 175.

[13] M. Asano, H. D. Kim, R. Kitano, and Y. Shimizu, *Natural supersymmetry at the LHC*, Journal of High Energy Physics **2010** (2010) 1–17.

[14] ATLAS Collaboration, *ATLAS Run 1 searches for direct pair production of third-generation squarks at the Large Hadron Collider*, Eur. Phys. J. C **75** (2015) 510, arXiv:1506.08616 [hep-ex].

[15] CMS Collaboration, *Search for top-squark pair production in the single-lepton final state in pp collisions at* $\sqrt{s} = 8$ *TeV*, Eur. Phys. J. C **73** (2013) 2677, arXiv:1308.1586 [hep-ex].

[16] CMS Collaboration, *Search for supersymmetry using razor variables in events with b-tagged jets in pp collisions at* $\sqrt{s} = 8$ *TeV*, Phys. Rev. D **91** (2015) 052018, arXiv:1502.00300 [hep-ex].

[17] CMS Collaboration, *Searches for supersymmetry using the* M_{T2} *variable in hadronic events produced in pp collisions at* 8 *TeV*, JHEP **1505** (2015) 078, arXiv:1502.04358 [hep-ex].

[18] CMS Collaboration, *Searches for third-generation squark production in fully hadronic final states in proton–proton collisions at* $\sqrt{s} = 8$ *TeV*, JHEP **1506** (2015) 116, arXiv:1503.08037 [hep-ex].

[19] CMS Collaboration, *Search for direct pair production of scalar top quarks in the single- and dilepton channels in proton–proton collisions at* $\sqrt{s} = 8$ *TeV*, arXiv:1602.03169 [hep-ex].

[20] K. Inoue, A. Kakuto, H. Komatsu, and S. Takeshita, *Aspects of Grand Unified Models with Softly Broken Supersymmetry*, Prog. Theor. Phys. **68** (1982) 927, [Erratum: Prog. Theor. Phys.70,330(1983)].

[21] J. R. Ellis and S. Rudaz, *Search for Supersymmetry in Toponium Decays*, Phys. Lett. B **128** (1983) 248.

[22] ATLAS Collaboration, *Search for direct top squark pair production in final states with two tau leptons in pp collisions at* $\sqrt{s} = 8$ *TeV with the ATLAS detector*, Eur. Phys. J. C **76** (2016) 81, arXiv:1509.04976 [hep-ex].

[23] The LEP SUSY Working Group and ALEPH, DELPHI, L3, OPAL experiments, *Combined LEP selectron/smuon/stau results, 183-208 GeV*, http://lepsusy.web.cern.ch/lepsusy/www/sleptons_summer04/slep_final.html, Mar., 2016.

[24] ATLAS Collaboration, *The ATLAS Experiment at the CERN Large Hadron Collider*, JINST **3** (2008) S08003.

[25] ATLAS Collaboration, *ATLAS Insertable B-Layer Technical Design Report*, CERN-LHCC-2010-013. ATLAS-TDR-19, 2010, http://cds.cern.ch/record/1291633.

[26] ATLAS Collaboration, *2015 start-up trigger menu and initial performance assessment of the ATLAS trigger using Run-2 data*, ATL-DAQ-PUB-2016-001, 2016, https://cds.cern.ch/record/2136007/.

[27] ATLAS Collaboration, *Improved luminosity determination in pp collisions at* $\sqrt{s} = 7$ *TeV using the ATLAS detector at the LHC*, Eur. Phys. J. C **73** (2013) 2518, arXiv:1302.4393 [hep-ex].

[28] ATLAS Collaboration, *Luminosity determination in pp collisions at* $\sqrt{s} = 8$ *TeV using the ATLAS detector at the LHC*, to be submitted to Eur. Phys. J. C.

[29] J. Alwall, R. Frederix, S. Frixione, V. Hirschi, F. Maltoni, O. Mattelaer, H. S. Shao, T. Stelzer, P. Torrielli, and M. Zaro, *The automated computation of tree-level and next-to-leading order differential cross sections, and their matching to parton shower simulations*, JHEP **07** (2014) 079, arXiv:1405.0301 [hep-ph].

[30] R. D. Ball et al., *Parton distributions with LHC data*, Nucl. Phys. **B867** (2013) 244–289, arXiv:1207.1303 [hep-ph].

[31] T. Sjostrand, S. Mrenna, and P. Z. Skands, *A Brief Introduction to PYTHIA 8.1*, Comput. Phys. Commun. **178** (2008) 852–867, arXiv:0710.3820 [hep-ph].

[32] D. J. Lange, *The EvtGen particle decay simulation package*, Nucl. Instrum. Meth. **A462** (2001) 152–155.

[33] W. Beenakker, M. Kramer, T. Plehn, M. Spira, and P. M. Zerwas, *Stop production at hadron colliders*, Nucl. Phys. **B515** (1998) 3–14, hep-ph/9710451.

[34] W. Beenakker, S. Brensing, M. Kramer, A. Kulesza, E. Laenen, and I. Niessen, *Supersymmetric top and bottom squark production at hadron colliders*, JHEP. **1008** (2010) 098, arXiv:1006.4771 [hep-ph].

[35] W. Beenakker, S. Brensing, M. Kramer, A. Kulesza, E. Laenen, et al., *Squark and gluino hadroproduction*, Int.J.Mod.Phys. **A26** (2011) 2637–2664, arXiv:1105.1110 [hep-ph].

[36] M. Kramer, A. Kulesza, R. van der Leeuw, M. Mangano, S. Padhi, et al., *Supersymmetry production cross sections in pp collisions at* $\sqrt{s} = 7$ *TeV*, arXiv:1206.2892 [hep-ph].

[37] S. Alioli, P. Nason, C. Oleari, and E. Re, *A general framework for implementing NLO calculations in shower Monte Carlo programs: the POWHEG BOX*, JHEP **06** (2010) 043, arXiv:1002.2581 [hep-ph].

[38] H.-L. Lai, M. Guzzi, J. Huston, Z. Li, P. M. Nadolsky, J. Pumplin, and C. P. Yuan, *New parton distributions for collider physics*, Phys. Rev. **D82** (2010) 074024, arXiv:1007.2241 [hep-ph].

[39] P. Z. Skands, *Tuning Monte Carlo Generators: The Perugia Tunes*, Phys. Rev. **D82** (2010) 074018, arXiv:1005.3457 [hep-ph].

[40] T. Sjostrand, S. Mrenna, and P. Z. Skands, *PYTHIA 6.4 Physics and Manual*, JHEP **05** (2006) 026, arXiv:hep-ph/0603175 [hep-ph].

[41] M. Czakon and A. Mitov, *Top++: A Program for the Calculation of the Top-Pair Cross-Section at Hadron Colliders*, Comput. Phys. Commun. **185** (2014) 2930, arXiv:1112.5675 [hep-ph].

[42] N. Kidonakis, *Two-loop soft anomalous dimensions for single top quark associated production with a W- or H-*, Phys. Rev. **D82** (2010) 054018, arXiv:1005.4451 [hep-ph].

[43] P. Kant, O. M. Kind, T. Kintscher, T. Lohse, T. Martini, S. Mölbitz, P. Rieck, and P. Uwer, *HatHor for single top-quark production: Updated predictions and uncertainty estimates for single top-quark production in hadronic collisions*, Comput. Phys. Commun. **191** (2015) 74–89, arXiv:1406.4403 [hep-ph].

[44] T. Gleisberg, S. Hoeche, F. Krauss, M. Schonherr, S. Schumann, F. Siegert, and J. Winter, *Event generation with SHERPA 1.1*, JHEP **02** (2009) 007, arXiv:0811.4622 [hep-ph].

[45] S. Hoeche, F. Krauss, M. Schonherr, and F. Siegert, *QCD matrix elements + parton showers: The NLO case*, JHEP **04** (2013) 027, arXiv:1207.5030 [hep-ph].

[46] ATLAS Collaboration, *ATLAS Pythia 8 tunes to* 7 *TeV data*, ATL-PHYS-PUB-2014-021, 2014, http://cdsweb.cern.ch/record/1966419.

[47] A. Lazopoulos, T. McElmurry, K. Melnikov, and F. Petriello, *Next-to-leading order QCD corrections to* $t\bar{t}Z$ *production at the LHC*, Phys. Lett. **B666** (2008) 62–65, arXiv:0804.2220 [hep-ph].

[48] J. M. Campbell and R. K. Ellis, $t\bar{t}W^{+-}$ *production and decay at NLO*, JHEP **07** (2012) 052, arXiv:1204.5678 [hep-ph].

[49] G. Corcella, I. G. Knowles, G. Marchesini, S. Moretti, K. Odagiri, P. Richardson, M. H. Seymour, and B. R. Webber, *HERWIG 6: An Event generator for hadron emission reactions with interfering gluons (including supersymmetric processes)*, JHEP **01** (2001) 010, arXiv:hep-ph/0011363 [hep-ph].

[50] M. H. Seymour and A. Siodmok, *Constraining MPI models using σ_{eff} and recent Tevatron and LHC Underlying Event data*, JHEP **10** (2013) 113, arXiv:1307.5015 [hep-ph].

[51] J. Pumplin, D. R. Stump, J. Huston, H. L. Lai, P. M. Nadolsky, and W. K. Tung, *New generation of parton distributions with uncertainties from global QCD analysis*, JHEP **07** (2002) 012, arXiv:hep-ph/0201195 [hep-ph].

[52] S. Dittmaier et al., *Handbook of LHC Higgs Cross Sections: 2. Differential Distributions*, arXiv:1201.3084 [hep-ph].

[53] GEANT4 Collaboration, S. Agostinelli et al., *GEANT4: A Simulation toolkit*, Nucl. Instrum. Meth. **A506** (2003) 250–303.

[54] ATLAS Collaboration, *The ATLAS Simulation Infrastructure*, Eur. Phys. J. C **70** (2010) 823, arXiv:1005.4568 [hep-ex].

[55] ATLAS Collaboration, *The simulation principle and performance of the ATLAS fast calorimeter simulation FastCaloSim*, ATL-PHYS-PUB-2010-013, CERN, Geneva, Oct, 2010. https://cds.cern.ch/record/1300517.

[56] ATLAS Collaboration, *Electron efficiency measurements with the ATLAS detector using the 2015 LHC proton-proton collision data*, ATLAS-CONF-2016-024, CERN, Geneva, Jun, 2016. https://cds.cern.ch/record/2157687.

[57] ATLAS Collaboration, *Muon reconstruction performance of the ATLAS detector in proton–proton collision data at $\sqrt{s}$ = 13 TeV*, Eur. Phys. J. C **76** (2016) 292, https://cds.cern.ch/record/2139897.

[58] M. Cacciari, G. P. Salam, and G. Soyez, *The anti-k_T jet clustering algorithm*, JHEP **04** (2008) 063, arXiv:0802.1189 [hep-ph].

[59] ATLAS Collaboration, *Jet Calibration and Systematic Uncertainties for Jets Reconstructed in the ATLAS Detector at $\sqrt{s}$ = 13 TeV*, ATL-PHYS-PUB-2015-015, CERN, Geneva, Jul, 2015. https://cds.cern.ch/record/2037613.

[60] ATLAS Collaboration, *Tagging and suppression of pileup jets with the ATLAS detector*, ATLAS-CONF-2014-018, CERN, Geneva, May, 2014. https://cds.cern.ch/record/1700870.

[61] ATLAS Collaboration, *Performance of b-Jet Identification in the ATLAS Experiment*, JINST **11** (2016) P04008, arXiv:1512.01094 [hep-ex].

[62] ATLAS Collaboration, *Expected performance of the ATLAS b-tagging algorithms in Run-2*, ATL-PHYS-PUB-2015-022, CERN, Geneva, Jul, 2015. https://cds.cern.ch/record/2037697.

[63] ATLAS Collaboration, *Optimisation of the ATLAS b-tagging performance for the 2016 LHC Run*, ATL-PHYS-PUB-2016-012, CERN, Geneva, Jun, 2016. https://cds.cern.ch/record/2160731.

[64] ATLAS Collaboration, *Reconstruction, Energy Calibration, and Identification of Hadronically Decaying Tau Leptons in the ATLAS Experiment for Run-2 of the LHC*, ATL-PHYS-PUB-2015-045, CERN, Geneva, Nov, 2015. https://cds.cern.ch/record/2064383.

[65] ATLAS Collaboration, *Performance of missing transverse momentum reconstruction for the ATLAS detector in the first proton-proton collisions at* $\sqrt{s}$ = 13 TeV, ATL-PHYS-PUB-2015-027, CERN, Geneva, Jul, 2015. https://cds.cern.ch/record/2037904.

[66] S. K. Boutle, A. M. Wharton, O. Arnaez, D. Schaefer, F. Meloni, J. D. Mansour, and S. Pagan Griso, *Vertex Reconstruction Performance of the ATLAS Detector at* $\sqrt{s}$ = 13 *TeV*, ATL-PHYS-PUB-2015-026, CERN, Geneva, Jul, 2015. https://cds.cern.ch/record/2037717.

[67] C. G. Lester and D. J. Summers, *Measuring masses of semi-invisibly decaying particles pair produced at hadron colliders*, arXiv:hep-ph/9906349.

[68] A. Barr, C. Lester, and P. Stephens, *m(T2) : The Truth behind the glamour*, J. Phys. **G29** (2003) 2343–2363, arXiv:hep-ph/0304226.

[69] C. G. Lester and B. Nachman, *Bisection-based asymmetric MT2 computation: a higher precision calculator than existing symmetric methods*, arXiv:1411.4312 [hep-ph].

[70] M. Baak, G. Besjes, D. Côte, A. Koutsman, J. Lorenz, et al., *HistFitter software framework for statistical data analysis*, Eur. Phys. J. **C75** (2015) 153, arXiv:1410.1280 [hep-ex].

[71] G. Cowan, K. Cranmer, E. Gross, and O. Vitells, *Asymptotic formulae for likelihood-based tests of new physics*, Eur. Phys. J. **C71** (2011) 1554, arXiv:1007.1727 [physics.data-an], [Erratum: Eur. Phys. J. **C73** (2013) 2501].

[72] A. L. Read, *Presentation of search results: The CL(s) technique*, J.Phys.G **G28** (2002) 2693–2704.

A. Appendix

Table 6 shows the expected event yields and selection efficiencies of the requirements constituting the signal region.

$m(\tilde{t}_1)$ [GeV], $m(\tilde{\tau}_1)$ [GeV]	700, 190		700, 540	
	N	ε_1	N	ε_1
generated events with ≥ 1 e/μ	477.8	–	502.0	–
event cleaning	460.1	96.3 %	478.6	95.3 %
≥ 1 τ_{had}	182.8	39.7 %	209.4	43.7 %
single-lepton trigger	49.9	27.3 %	81.3	38.8 %
at least one signal e/μ	36.4	72.9 %	57.4	70.6 %
veto additional e/μ and τ_{had}	35.8	98.4 %	55.6	97.0 %
opposite-sign requirement	35.1	98.0 %	53.6	96.3 %
≥ 2 jets, leading jet $p_{\mathrm{T}} > 50$ GeV	34.8	99.3 %	48.7	90.8 %
≥ 1 b-tagged jet	32.5	93.4 %	44.2	90.9 %
$E_{\mathrm{T}}^{\mathrm{miss}} > 180$ GeV	22.1	68.0 %	26.6	60.2 %
$p_{\mathrm{T}}(\tau_{had}) > 70$ GeV	12.4	56.1 %	23.0	86.4 %
$m_{\mathrm{T2}}(\ell, \tau) > 100$ GeV	4.2	33.7 %	17.1	74.4 %

Table 6: Number of expected signal events N at different stages of the signal-region selection for two signal benchmark points and relative selection efficiency ε_1 of each requirement. The numbers are normalised to 13.2 fb^{-1}.